Northern high latitude heat budget decomposition and transient warming

Maria A. A. Rugenstein,

Department of Physics and Astronomy, Utrecht University, Utrecht, Netherlands

Michael Winton,* Ronald J. Stouffer

Stephen M. Griffies, Robert Hallberg

Geophysical Fluid Dynamics Laboratory/NOAA, Princeton, New Jersey

Corresponding author address: Dr. Michael Winton, NOAA/GFDL, Princeton University Forrestal Campus, 201 Forrestal Rd., Princeton, NJ 08540.

E-mail: Michael.Winton@noaa.gov

ABSTRACT

Many climate models are unable to capture the magnitude of observed warming and sea ice decline in high northern latitudes. To understand the factors affecting the simulated warming we compare the response to increasing CO_2 in two pairs of climate models by decomposing the 40–90°N region heat budget. Each pair includes a member with enhanced global and northern high latitude surface temperature increase and smaller ocean heat uptake efficiency compared with its counterpart member. Significant differences in sensitivity can be traced to formulation differences between the model pairs. The difference in surface heat flux perturbation between the models is the main forcing of the differences in temperature increase and ocean heat uptake. Atmospheric heat transport and outgoing longwave radiation counteract the model differences in northern high latitude warming while shortwave radiation differences enhance it. The surface flux perturbation difference is associated with a difference in the North Atlantic ocean convection in the control climates: When Labrador Sea convection is present in the control, it weakens in the perturbed climate leading to a larger reduction in ocean overturning and heat transport to northern high latitudes, a relatively cooler high latitude ocean surface, increased ocean heat uptake, and a reduction in high latitude atmospheric warming compared to the model counterpart with stable Labrador Sea convection. Because the 40–90°N region accounts for up to 40% of the global ocean heat uptake the process described here may substantially influence the global heat uptake efficiency.

1. Introduction

The ocean buffers atmospheric warming by absorbing and storing heat in a warming climate. Ocean dynamical mechanisms are thought to influence the ocean heat storage (e.g., Herweijer et al. 2005; Banks and Gregory 2006; Xie and Vallis 2011). Climate models differ in describing the atmospheric warming (climate sensitivity), the amount of heat taken up by the oceans, the degree of ocean circulation changes, and the way the atmosphere responds to the ocean heat uptake (e.g. Raper et al. 2002; Knutti and Tomassini 2008; Winton et al. 2010). We use closely related models to trace differences in the climate warming response to specific differences stemming from the ocean response.

One prominent pattern of atmospheric warming in models and observations is the amplification of high latitude temperature increase compared to the global mean (e.g. Manabe and Stouffer 1979; Hansen et al. 2010). Although often referred to as Arctic amplification, the enhanced temperature increase is also apparent in sub-Arctic regions (Holland and Bitz 2003, their Figure 1). Climate models analyzed for the Climate Model Intercomparison Project Phase 3 (CMIP3) differ in the amplitude of Arctic amplification, spanning a range of 1.2 to 2.4 at the time of CO_2 doubling (Winton 2006). There have been various attempts to explain the amplification across models, mostly focussing on the surface albedo feedback (SAF) and the atmospheric heat transport responses to increased radiative forcing (e.g., Holland and Bitz 2003; Fletcher et al. 2009; Graversen and Wang 2009; Screen and Simmonds 2010). As an example Mahlstein and Knutti (2011) showed that models with a large northward ocean heat transport in the control climate have an enhanced sea ice cover reduction in perturbed simulations.

Atmosphere-Ocean general circulation models (AOGCMs) and Earth system models of intermediate complexity (EMICs) indicate that in a warming climate the Atlantic meridional overturning circulation (AMOC) weakens (Meehl et al. 2007). Changes in temperature and salinity cause a more stable, less convective North Atlantic, suppressing the AMOC. Using AOGCMs and EMICs Gregory et al. (2005) show changes in surface heat flux dominate freshwater fluxes in forcing AMOC weakening (their Figure 4). However, changes in freshwater supply and the sensitivity of the AMOC to freshwater supply differ greatly between these models and explain in part the large inter-model spread in AMOC response to radiative forcing (Stouffer et al. 2006c). Furthermore, Gregory et al. (2005) show that models with initially stronger AMOCs tend to show an enhanced weakening compared to models with initial weaker AMOCs (their Figure 3).

Weaver et al. (2007) confirmed the results of Gregory et al. (2005) with an EMIC intra-model analysis and found that the response of the AMOC to freshwater and heat fluxes depends on the mean climate state. In cold control climates, freshwater fluxes counteracted AMOC weakening; in warm control climates, they enhanced it. The transition took place at the onset of the Labrador Sea convection, which occurs in the model of Weaver et al. (2007) between 240 and 260 ppmv CO_2 forcing. They speculate that the existence of Labrador Sea convection in a model might precondition its transient AMOC response.

Another approach to the correlation between initial AMOC strength and the magnitude of its decrease was taken by Levermann et al. (2007), proposing that initially weaker AMOCs associated with an initially large sea ice cover are stabilized via the SAF. Enhanced ocean heat loss in regions where sea ice retreats would cool the ocean surface layers and allow for enhanced convection. Thus initially weaker AMOCs would decrease, but not as much

as their initially strong counterparts with a comparatively small ice cover. Gregory and Tailleux (2010) take a dynamical approach to the problem, interpreting the AMOC decrease with a conceptual model that connects changes in circulation to the kinetic energy balance. Hence a reduced input of kinetic energy from reduced deep water formation in the North Atlantic is balanced by reduced dissipation of kinetic energy, i.e., a weakening of the AMOC.

We are concerned with identifying factors that lead to differences in northern high latitude warming between climate models. The response of the AMOC to climate forcing plays a crucial role due to the close connection between its strength and the ocean heat transport. In Section 2 we introduce the experimental set up and the decomposition of high latitude heat fluxes. Section 3 presents the results of the heat budget analysis and some related model features. We discuss the implications of the results in Section 4.

2. Models and Methods

a. Models

We use two versions of two different AOGCMs, respectively. The first pair of climate models are GFDL CM2.0 and CM2.1. These models were used for the Intergovernmental Panel on Climate Change Fourth Assessment Report (IPCC AR4) and are fully described by Griffies et al. (2005); Delworth et al. (2006) and Gnanadesikan et al. (2006), with further analyses done by Wittenberg et al. (2006) and Stouffer et al. (2006b). The second pair are two versions of GFDL's newly developed Earth System Model ESM2G described by Dunne et al. (subm.). We use ESM2G which contributes to the CMIP5 database, as well as a preliminary

version referred to here as ESM2preG. A short model description and comparison is given below. The reader is referred to the publications already mentioned for further details.

Table 1 gives an overview of the different climate models and their components. CM2.0 and CM2.1 share the same land model and sea ice model. Likewise, ESM2G and ESM2preG use the same land and sea ice models, though the land model is updated from the earlier version used in CM2.0/CM2.1, and the sea ice model albedos have been set to more physically appropriate values. The ocean model configurations in CM2.0 and CM2.1 differ in the lateral subgrid scale parameterizations for friction and neutral diffusion, with the CM2.1 settings leading to a stronger subpolar gyre circulation and poleward ocean heat transport. CM2.0 and CM2.1 use different atmospheric dynamical cores, with CM2.0 using the B-grid core from GFDL GAMDT (2004), whereas CM2.1 uses the finite volume core of Lin (2004). ESM2G and ESM2preG use very nearly the same atmospheric model as CM2.1, and all models use an atmospheric resolution nominally around 2°. The two ESMs share the land model as well, but ESM2G has a 20 % reduced total biomass due to an other land vegetation tuning. Both ESMs use Generalized Ocean Layer Dynamics (GOLD) with four bulk mixed and buffer layers and 59 interior isopycnal layers (Dunne et al. subm.). The major differences between the two ESMs are the introduction of geothermal heating and increased diapycnal mixing in ESM2G compared to ESM2preG, both added to address a cool drift in the deep ocean of ESM2preG. Since ESM2preG and ESM2G use the same atmospheric component we can attribute their perturbation differences to one model component, the ocean. All four models use approximately 1° (refined in equatorial areas) grid resolution for the ocean.

b. Experiments

We report on two integrations of each model. The first experiment is a "mean climate" or control run with 1860 forcing. Atmospheric CO_2 concentrations are held constant at 286 ppm. The second experiment includes a forcing of 1% CO_2 increase each year beginning in year 1860 from the initial condition prescribed by the control experiment. This idealized scenario is a standard to compare model behavior (Manabe et al. 1991; Meehl et al. 2000). We do not aim for predictions of the future real world climate state or comparisons to historical observations. Nonetheless the 1% CO_2 forcing is linearly transferable to prevalent non-intervention scenario projections (Knutti and Tomassini 2008). The CO_2 mixing ratio quadruples from 286 ppm to 1144 ppm in year 140 and then stays constant. Non-CO_2 forcing agents are held constant at their 1860 values.

In order to minimize the effect of intrinsic model internal climate variability and seasonality we always average over the first hundred years of each run. The pertinent variables obtained by averaging are robust features of the climate system. Since radiative forcing, temperature and sea ice responses are approximately linear in time, all variables can be multiplied by 1.4 (=70 yrs/50 yrs) to obtain an equivalent transient response for the variable at the time of doubling CO_2 around year 70. We use the expressions "response" or "perturbation" to express the difference between the transient forced and the control integration. The assumption is, that if there is a climate drift in the control run, it is present in the forced run with the same strength, and makes no contribution to the differences between the two runs. In the following we do not deal with equilibrium states, but exclusively with transient responses.

c. Heat budget decomposition

In order to analyze the atmospheric and oceanic temperature increase, and the amplification of high latitude temperature increase in particular, we decompose the heat budget into the processes schematically shown in Figure 1. The region between 40 and 90°N is evaluated, including the Arctic and a broad sub-Arctic region. We choose the lower bound of 40°N because the net poleward energy transport and the control climate AMOC strength are largest there (e.g., Trenberth and Caron 2001; Mayer and Haimberger 2011). In addition in Section 3 it will become clear that across our models the decrease of the AMOC, the associated decrease in ocean northward heat transport, and the intra-model variability of the same, have a maximum at 35 – 40°N. Furthermore the zonal atmospheric vertical temperature response shows a pattern with different regimes north and south of roughly 40°N (Stouffer et al. 2006b; Meehl et al. 2007, their Figure 10.7). Namely south of 40°N the upper tropospheric warming is largest, whereas north of 40°N the surface temperature increase is most pronounced and larger than the global mean. Winton (2006) shows that although the temperatures of the sub-Arctic regions show only a slightly amplified temperature response relative to the global mean, the standard deviation to mean warming between CMIP3 models is nearly the same as for the Arctic region, indicating that the AOGCMs struggle in representing the sub-Arctic region in the same way as they do in representing the Arctic region.

The absorbed shortwave radiation (SW) and outgoing longwave radiation (OLR) can be differenced to obtain the net downward top of the atmosphere (TOA) radiation flux. Equation (1) displays the net downward surface heat flux (SFC) in the notation of Peixoto

and Oort (1992), with $F_{SW}^{\uparrow\downarrow}$ being the net surface shortwave radiation flux, $F_{LW}^{\uparrow\downarrow}$ the net surface longwave radiation flux, $F_{SH}^{\uparrow\downarrow}$ the net surface sensible heat flux, finally F_{LH} the latent heat flux resulting from evaporation and F_M the latent heat flux resulting from melting snow

$$F_{sfc}^{\uparrow\downarrow} = F_{SW}^{\uparrow\downarrow} + F_{LW}^{\uparrow\downarrow} - F_{SH}^{\uparrow\downarrow} - F_{LH} - F_M \tag{1}$$

.

Throughout our analysis heat fluxes contain latent components. The convergence of atmospheric heat transport ($-\nabla \cdot AHT$) through 40°N is approximated as the residual of net surface and TOA fluxes, i.e., $F_{sfc}^{\uparrow\downarrow}$ and $F_{TOA}^{\uparrow\downarrow}$ respectively. We diagnose it assuming the atmosphere has no heat capacity:

$$\frac{dE_A}{dt} = F_{TOA}^{\uparrow\downarrow} - F_{sfc}^{\uparrow\downarrow} - \nabla \cdot AHT \approx 0 \tag{2}$$

The ocean heat transport (OHT) through 40°N includes the effect of large scale advection resolved by the model, and parameterized subgrid scale mesoscale and sub-mesoscale eddy transport. The sub-grid parameterizations and bottom and top boundary conditions are formulated differently for each model (Griffies et al. 2005; Delworth et al. 2006; Gnanadesikan et al. 2006; Dunne et al. subm.). The ocean heat storage (OHS) is calculated as the volume integral of $\rho_o \, c_p \, \theta$ for the ocean model, where $\rho_o = 1035\,\mathrm{kg/m^3}$ is the reference density for the Boussinesq approximation, $c_p = 3992\,\mathrm{J/(kgC)}$ is the specific heat capacity for seawater, and θ is the potential temperature. The ocean heat transport and perturbation in ocean heat storage are then divided by the Earth's surface area between 40 and 90°N in order to compare it to the $\mathrm{W/m^2}$ unit of the other fluxes. We note that the method for calculating the

storage is approximate because averaged temperatures are used to represent the boundaries of the averaging interval. This accounts for the small differences between the divergence of boundary fluxes and estimated heat storage evident in Figures 2 and 7.

Our heat budget analysis accounts for the zonally averaged 40–90°N ocean. However, features such as the slowdown of the overturning circulation or the perturbation of surface heat fluxes are most pronounced in the North Atlantic. Unless otherwise noted our analyses are 40–90°N zonal means dominated by the North Atlantic signal, which we do not show separately. Similar heat budget studies have been performed using CMIP3 models e.g. by Winton (2008) and Lu and Cai (2009) or using observations e.g. by Trenberth and Stepaniak (2004).

3. Model comparison

Figure 2a depicts the processes shown in Figure 1 in the form of the average control run fluxes of the four models. The atmospheric contribution of the northward energy transport is five times greater than the oceanic contribution. The ocean heat storage is close to zero, reflecting a near equilibrium state. The average surface flux between 40 and 90°N is 9.9 $\mathrm{W/m^2}$ and directed from the ocean to the atmosphere. The OLR balances the overall northward heat transport, surface, and absorbed shortwave fluxes. The simulated and observed partitioning of heat fluxes are similar: Trenberth and Caron (2001) estimate the atmospheric heat transport at 43°N to account for 78 % of the net transport, our model mean accounts for 83 % in good agreement. Through 40°N our model's control climate ocean heat transport ranges from 0.6 to 1 Petawatt (not shown), while Trenberth and Caron (2001) report

on estimates of 0.5 to 1.2 Petawatts. For a detailed evaluation of our four models against observations we refer to Stouffer et al. (2006b); Delworth et al. (2006); Gnanadesikan et al. (2006) and Dunne et al. (subm.).

Figure 2b shows the model average response to the forcing, i.e., the difference between perturbed and control runs. The high latitude surface air temperature (T_s) between 40 and 90°N increases on average by 1.6 K, while the global mean surface air temperature rise is 1.1 K under an average 2.5 W/m^2 global CO_2 radiative forcing. Increases in SW flux and the atmospheric heat transport enhance the warming, while the OLR and the surface heat flux perturbations damp it. The atmospheric heat transport increase is explained by Held and Soden (2006) as a response of latent heat transport to warming. Zelinka and Hartmann (2011) discuss a pathway by which feedbacks pronounced in low latitudes impact and enhance the meridional poleward heat transport and can affect the energy budget at remote places. We show later that atmospheric heat convergence also balances the energy fluxes in the high latitude region.

All four of our models agree on the sign of the flux perturbations (not shown). The surface heat flux, upward in the controls (i.e., ocean to atmosphere), is reduced by 1.41 W/m^2 and must be balanced by changes in ocean heat storage (increased by 0.2 W/m^2) and ocean heat transport (reduced by 1.01 W/m^2). Therefore the storage accounts for about a fifth of the surface flux perturbation.

Figure 3 shows the perturbed climate AMOC responses of each model. The annual maximum value of the meridional volume transport, vertically integrated between the surface and the bottom at 40°N (in Sverdrups, where 1 Sv is equivalent to $10^6 m^3 s^{-1}$), was calculated in depth space for the ESM2preG/G models and includes sub-grid scale mixing parameteriza-

tion (Gent and Mcwilliams 1990) for CM2.0 and CM2.1. The AMOC loses strength linearly in time until year 140, when CO_2 is capped at quadrupling. The AMOC recovers slightly when CO_2 concentrations are held constant beyond the year 140 of the model integration (for details on CM2.0 and CM2.1 integrations see Stouffer et al. 2006b). We note that the linearity of the overturning decline over the first century supports our use of averages over this century in our analysis. The fact that models with a strong overturning in the control run, like CM2.1 and ESM2G, show a bigger overturning reduction than models with initially weaker overturning, like CM2.0 and ESM2preG, is consistent with the relationship found by Gregory et al. (2005). The relative magnitudes of our AMOC reduction under CO_2 forcing is in the range of the models analyzed by Gregory et al. (2005) (see their Figure 3): The correlation coefficient of initial AMOC strength and AMOC strength reduction is 0.7 for our four models, 0.74 for AOGCMs and EMICs analyzed by Gregory et al. (2005), 0.63 in EMICs analyzed by Levermann et al. (2007) and 0.87 in the intra-model analysis of one EMIC by Weaver et al. (2007). The ordinary least square linear regression is calculated with the AMOC reduction at the time of CO_2 quadrupling as the dependent variable and the control climate AMOC strength as the independent variable, both in Sv. The corresponding slope of our models is -0.66, with the models used by Gregory et al. (2005) having a value of -0.45. Although our correlation and regression are derived from just four models, the relationships between control overturning and overturning response in the small ensemble studied here confirm the relationships in larger ensembles studied previously.

The impact of the control overturning strength and the overturning decline is expected to be evident in poleward heat transport, with stronger heat transport reduction in models with stronger overturning decline. Figure 4 illustrates the perturbation of the zonal in-

tegrated annual mean ocean northward heat transport. The differences in the control run North Atlantic heat transport (not shown) reflect the different initial AMOC strengths, with CM2.1 and ESM2G having the stronger and CM2.0 and ESM2preG having the weaker ocean heat transport and AMOC through 40°N. Averaging the perturbation of the four models at 40°N gives the OHT arrow in Figure 2b. The heat transport perturbation is particularly variable among models around 40°N. Models with a stronger control climate AMOC and a stronger overturning decline (CM2.1 (blue) and ESM2G (black)) show a stronger reduction of northward heat transport relative to their weaker overturning counterparts CM2.0 (green) and ESM2preG (red).

a. Labrador Sea

Figure 5 shows the average wintertime mixed layer depths, which can be used as a measure of convection and is defined as the depth where the buoyancy difference with respect to the surface level is greater or equal to 3×10^{-4} m s^{-2} (Stouffer et al. 2006b). The upper four panels show the control run of each model, corresponding to Figure 2a, while the lower four panels show the responses to CO_2 forcing, corresponding to Figure 2b. Only the North Atlantic is depicted for its most pronounced convective sites. The mixed layer depths are reduced almost everywhere upon CO_2 forcing, but focusing on the small scale details of the upper panel of Figure 5, it becomes clear that our two pairs of closely related models differ strongly in strength and location of their northern convective sites. The control climate wintertime Labrador Sea convection is the prominent difference: CM2.0 and ESM2preG on the left hand side have very little or no Labrador Sea convection, while CM2.1 and ESM2G

show deeper mixed layer depths, i.e., stronger convection. The bottom panels of Figure 5 demonstrate that in the Labrador Sea only the models with control climate convection experience a reduction of the convection. We confirm the findings of Wood et al. (1999), Stouffer et al. (2006b) and Weaver et al. (2007) who point out that the behavior of the AMOC decline strongly depends on the reduction of the Labrador Sea convection *if* the model control runs have it. Comparing Figure 5 and 3 indicates that initially strong Labrador Sea convection (in CM2.1 (blue) and ESM2G (black) on the right hand of Figure 5 (Figure 3)) is associated with an initially stronger AMOC. The same models show a stronger AMOC decline than their model counterparts, which is consistent with the reduction of Labrador Sea convection.

b. Climate sensitivity

The general picture of the temperature response due to increased radiative forcing becomes clear in Figure 6 which shows the global zonal averages of air and water temperature response for each model. The most robust features are the overall warming of the atmosphere with maxima in the low latitude upper troposphere and at the northern high latitude surface, as well as the warming of the ocean surface layers. A 50–70°N surface and deep ocean cooling is most pronounced in ESM2G which experiences the strongest decline in overturning and thereby the strongest heat transport reduction (compare also Figure 3 and Figure 4). While the ocean heat storage is discussed below, we note here that the cooling deep ocean volume around 70°N apparent in all four models is relatively small compared to the warming upper ocean volume around 40°N. A strong upper ocean warming feature around

70°N is noticeable in CM2.0 and ESM2preG which have a weak decline of the Labrador Sea convection as well as of the AMOC. The inter-model differences in the ocean warming are more pronounced than in the atmosphere.

The hemispheric asymmetry of the atmospheric temperature increase is a robust feature of climate models (e.g., Manabe and Stouffer 1979; Stouffer et al. 2006b) and observations (e.g., Hansen et al. 2010). The high latitude atmospheric warming is less in the Southern than in the Northern Hemisphere across all four models because of the smaller land fraction and stronger deep vertical mixing in the Southern ocean (Bryan et al. 1988). Between 90°S and 40°N the warming responses resemble each other and differ only in the extent of low latitude upper tropospheric warming and the vertical pattern of the Southern Hemispheric warming. However, between 40 and 90°N the tropospheric warming responses of the four models differ considerably. CM2.0 and ESM2preG show more extensive northern high latitude warming and more pronounced hemispheric asymmetry than CM2.1 and ESM2G.

The prominent features of Figure 6 are summarized in Table 2. All entries are, like the temperature fields in Figure 6, the differences of the hundred year averaged perturbed climate and the corresponding hundred year averaged control climate, as described in Section 2b. Again, assuming a roughly linear change of climate elements such as temperature, precipitation or sea ice retreat, one can multiply all entries by 1.4 to approximate the widely used transient response of the same variables (e.g., Gregory and Forster 2008; Winton 2008). The transient climate response (TCR) is defined as the global mean surface air temperature response at the time of doubled CO_2 in a model simulation with 1% CO_2 increase per year, i.e., a 20 year average centered around year 70 from the beginning of the perturbed run. Since the AOGCM is not in equilibrium at CO_2 doubling, the TCR depends on the ocean

heat uptake as well as the equilibrium climate sensitivity.

The global and 40–90°N average surface air temperature increases are shown in the first row of Table 2. Each model pair has one member (referred to in the following as the *more sensitive model*) with a large atmospheric temperature response, and one *less sensitive* member with a smaller response. The globally more sensitive members also experience a stronger increase of northern high latitude temperatures. The global ocean heat uptake shown in the second row is the change in TOA *or* surface heat flux, i.e., we assume the atmosphere to have no heat capacity and the overall global heat transport convergence is zero (Section 2c). The global ocean heat uptake efficiency, i.e., the ocean heat uptake normalized with the surface temperature increase, is smaller in each pair's more sensitive model (CM2.0 and ESM2preG) compared to its comparatively less sensitive counterpart (CM2.1 and ESM2G). The ocean heat uptake efficiency was introduced as a proportionality constant to relate the TCR linearly to the ocean heat uptake by Gregory and Mitchell (1997). Raper et al. (2002) find a positive relationship between temperature response and ocean heat uptake in a large group of GCMs.

Here the regional ocean heat uptake efficiency is calculated using the change in surface fluxes. To account for the northern high latitudes row four shows that the 40–90°N region takes up a substantial amount of heat compared with the remaining 90°S–40°N. The heat uptake and heat uptake efficiency in the 40–90°N region ranges from 16 % (in CM2.0) to 41 % (in ESM2G) of the global value. Previous work emphasized the impact of the Southern Ocean dynamics on the global heat uptake (Stouffer et al. 2006a). Here we emphasize the role of the North Atlantic. Its share of global ocean heat uptake efficiency is large enough to be important to the global efficiency differences.

The next to last row shows that the reduced warming in CM2.1 and ESM2G is also reflected in a smaller efficiency of the reduction in northern sea ice extent (the ice cover reduction per degree global warming). Winton (2011) discusses intermodel variations in this metric for IPCC AR4 models. In the Labrador Sea (not shown) the sea ice cover is reduced in the more sensitive model of each pair, i.e., CM2.0 and ESMpreG, while it increases slightly in the less sensitive models, i.e., CM2.1 and ESM2G.

Finally, the last row confirms Gregory et al. (2005) and summarizes Figure 3 in describing the reduction of the annual-mean maximum AMOC strength at 40°N for its initial strength (averaged over year 1-10, in Sv), its strength at CO_2 quadrupling (averaged over year 130 to 150, in Sv), and the reduction in percentage. In summary, column two and four show that the models with the strong control Labrador Sea convection, strong control overturning, and strong overturning decline are the ones with higher ocean heat uptake efficiency, smaller high latitude temperature amplification and a smaller sea ice extent reduction efficiency compared to their counterpart models.

c. High latitude temperature amplification

In Figure 7 we use the same region as in Figure 2a and b. Here the energy budget displays the difference of flux perturbations for each model pair:

$$\Delta\Delta F = (\Delta F)_{more\ sensitive\ model} - (\Delta F)_{less\ sensitive\ model}$$

where F is any of the fluxes or the heat storage depicted in Figure 1, the *more sensitive model*s are CM2.0 and ESM2preG with a stronger surface temperature increase, and the *less sensitive model*s are CM2.1 and ESM2G with a weaker surface temperature increase,

respectively. In other words: Figure 7 shows the *flux perturbation (ΔF) differences (Δ)* of each model pair. As an example the ocean heat transport reduction of 1.03 W/m^2 through 40°N in CM2.1 is subtracted from the ocean heat transport reduction of 0.28 W/m^2 in CM2.0. Thus the reduction in ocean heat transport in CM2.0 is 0.75 *smaller* than in CM2.1, and the OHT difference arrow in Figure 7a points north.

The main idea is to determine the cause of the temperature response differences. In both cases the enhanced temperature increase between 40 and 90°N is forced by the surface heat flux perturbation difference and amplified by the TOA SW perturbation difference. Both are marked by arrows pointing into the atmospheric part of the high latitude box in Figure 7a and b. On the other hand the atmospheric heat transport as well as the OLR flux differences, reflecting the difference in surface temperature, damp the temperature response differences, which is indicated by arrows pointing outwards. The difference in surface heat flux perturbation is consistent with the difference in oceanic heat transport perturbation, since the differences in heat storage between the models are very small (0.02 and 0.004 W/m^2). The response of the overturning circulation and associated change in ocean heat transport are, hence, important elements of high latitude climate change. Bitz et al. (2006) and Winton (2008) discuss a reverse pathway by which ice albedo feedback impacts ocean circulation. However, this pathway, which has an albedo reduction driving an overturning reduction, is counter to the model differences shown here, since a larger albedo reduction was associated with larger ocean heat uptake in these studies. It should be mentioned further that although the TOA SW and OLR perturbation differences have the same sign for both model pairs the net TOA radiation, i.e., $\Delta\Delta SW - \Delta\Delta OLR$ is negative

for ΔCM2.0 $-$ ΔCM2.1 but positive for ΔESM2preG $-$ ΔESM2G.

4. Discussion and concluding remarks

We have shown the surface heat flux response to radiative forcing to be important for the high latitude temperature amplification. Since the difference of ocean heat storage responses between our model pairs turns out to be negligible, it is the difference in northward heat transport responses which accounts for the difference in surface flux perturbation. In turn, the difference in ocean heat transport between the models is consistent with the magnitude of decreasing strength of the AMOC and the Labrador Sea convection.

With the Labrador Sea convection we have identified a small scale ocean dynamical mechanism which influences the heat uptake at Northern Hemispheric high latitudes (Wood et al. 1999; Weaver et al. 2007). This result confirms earlier findings that ocean dynamics plays a crucial role in heat uptake (Banks and Gregory 2006; Xie and Vallis 2011). In addition the Labrador Sea convection is a feature of the control climate that is important to the magnitude of AMOC response and hemispheric warming asymmetry (Stouffer et al. 2006b).

Table 2 and Figure 4 indicate that our models show a larger high latitude temperature amplification with initially weaker overturning and thus weaker northward heat transport reduction (CM2.0 and EMS2G) than their initially strong overturning counterparts (CM2.1 and ESM2G). This result is in contrast to the model analysis of Mahlstein and Knutti (2011), which suggests that models with an initially weaker ocean heat transport (in their case through 60°N, compare our Figure 4) would show less high latitude temperature am-

plification. We confirm the finding of Levermann et al. (2007) that models with initially weaker overturning experience a smaller surface heat flux response than their initially strong overturning counterparts. Levermann et al. (2007) argue that enhanced ocean heat loss would allow for more convection and thus stabilize the AMOC decrease. Counter to the EMIC analysis of Levermann et al (2007), the high latitude oceans in our models do not show enhanced ocean heat loss or enhanced convection. Instead, they show enhanced heat uptake and reduced convection (see Section 3). The same relationship is also valid for the 60–90°N region (not shown here) used by Levermann et al. (2007). Both Mahlstein and Knutti (2011) and Levermann et al. (2007) use the surface albedo feedback (SAF) as central point in their line of argumentation, either to explain the Arctic amplification or to explain the oceanic convection response and AMOC decrease.

In order to assess the importance of the SAF relative to the surface heat flux perturbation we analyze the TOA SW perturbation in detail (as e.g., Hall 2004; Graversen and Wang 2009). As described in Winton (2006) we separate the effect of the SAF and the non-SAF on the TOA SW perturbation. The analysis reveals that the model mean TOA SW perturbation is driven by the SAF induced enhanced ocean shortwave heat uptake, and damped by non-SAF (atmospheric) processes.

Table 3 shows a TOA SW break down, which clarifies that, in terms of high latitude temperature increase amplification, the non-SAF might act to reduce the temperature amplification difference (in the comparison of the CMs) or enhance it (in comparison of the ESMs). As also shown by Hall (2004), we conclude that the SAF should be used with caution in causal explanations of the high latitude temperature increase amplification and the AMOC reduction behavior. The models with larger SAF had smaller AMOC reductions. Since the

differences in surface heat flux can drive as well as be driven by the differences in AMOC response, we cannot determine causality. However, the formulation of the ESM2preG/G pair - with only the ocean mixing being substantially different - indicates an oceanic driver as a possible explanation for the differences. This is a rare opportunity to trace a significant change in sensitivities to formulation differences between the model components.

In Section 3c and Figure 7 we showed our model high latitude surface warming difference to be forced by the difference in surface heat flux perturbation and amplified by the differences in TOA SW SAF induced perturbation. Atmospheric heat transport and the OLR differences act to damp the high latitude temperature amplification, while the non-SAF contribution of the TOA SW perturbation might act either to damp or enhance differences.

Our results on the importance of the Labrador Sea convection may be sensitive to resolution because the Labrador Sea itself is only marginally resolved with the one degree ocean models used here. The distance between Cape Farewell and Newfoundland spans only twelve grid cells in our models (see Figure 5 and also Section 2b). The real world Labrador Sea convection is influenced by baroclinic eddies which form along the West Greenland coast and enable restratification. According to Jourdain et al. (2010) either a $1/15^{\circ}$ resolution or extremely accurate eddy parameterizations are needed to describe the Labrador sea convection appropriately.

Based on our results we emphasize the need for in-depth modeling studies to determine causal physical mechanisms. We suggest further investigation with high resolution eddy resolving ocean and climate models to represent the coupled interactions of sea ice and ocean circulation that remain to be understood in detail.

Acknowledgments.

We thank the developers of Geophysical Fluid Dynamics Laboratory models used here and gratefully acknowledge Isaac Held, Thomas Delworth, and Reto Knutti for comments on the manuscript.

REFERENCES

Banks, H. T. and J. M. Gregory, 2006: Mechanisms of ocean heat uptake in a coupled climate model and the implications for tracer based predictions of ocean heat uptake. *Geophys. Res. Lett.*, **33**, L07 608.

Bitz, C. M., P. R. Gent, R. A. Woodgate, M. M. Holland, and R. Lindsay, 2006: The influence of sea ice on ocean heat uptake in response to increasing CO_2. *Journal of Climate*, **19 (11)**, 2437–2450.

Bryan, K., S. Manabe, and M. J. Spelman, 1988: Interhemispheric Asymmetry in the Transient Response of a Coupled Ocean-Atmosphere Model to CO_2 Forcing. *Journal of Physical Oceanography*, **18 (8)**, 851–867.

Delworth, T. L., et al., 2006: GFDL's CM2 Global Coupled Climate Models. Part I: Formulation and Simulation Characteristics. *Journal of Climate*, **19 (5)**, 643–674.

Dunne, J. P., et al., subm.: GFDL's ESM2 global coupled climate-carbon Earth System Models Part I: Physical formulation and baseline simulation characteristics. *Journal of Climate*.

Fletcher, C. G., P. J. Kushner, A. Hall, and X. Qu, 2009: Circulation responses to snow albedo feedback in climate change. *Geophys. Res. Lett.*, **36 (9)**, L09 702.

Gent, P. R. and J. C. Mcwilliams, 1990: Isopycnal Mixing in Ocean Circulation Models. *Journal of Physical Oceanography*, **20 (1)**, 150–155.

GFDL GAMDT, 2004: The GFDL Global Atmospheric Model Development Team: The new GFDL global atmosphere and land model AM2/LM2: Evaluation with prescribed SST simulations. *Journal of Climate*, **17**, 4641–4673.

Gnanadesikan, A., et al., 2006: GFDL's CM2 Global Coupled Climate Models. Part II: The Baseline Ocean Simulation. *Journal of Climate*, **19 (5)**, 675–697.

Graversen, R. G. and M. Wang, 2009: Polar amplification in a coupled climate model with locked albedo. *Climate Dynamics*, **33**, 629–643.

Gregory, J. M. and P. M. Forster, 2008: Transient climate response estimated from radiative forcing and observed temperature change. *Journal of Geophysical Research*, **113**, D23 105.

Gregory, J. M. and J. F. B. Mitchell, 1997: The climate response to CO_2 of the Hadley Centre coupled AOGCM with and without flux adjustment. *Geophys. Res. Lett.*, **24 (15)**, 1943–1946.

Gregory, J. M. and R. Tailleux, 2010: Kinetic energy analysis of the response of the Atlantic meridional overturning circulation to CO_2-forced climate change. *Climate Dynamics*.

Gregory, J. M., et al., 2005: A model intercomparison of changes in the Atlantic thermohaline circulation in response to increasing atmospheric CO_2 concentration. *Geophys. Res. Lett.*, **32 (L12703)**.

Griffies, S. M., 2009: *Elements of MOM4p1: GFDL Ocean Group Technical Report No. 6*. NOAA/Geophysical Fluid Dynamics Laboratory, Princeton, USA, 444 pp.

Griffies, S. M., M. J. Harrison, R. C. Pacanowski, and A. Rosati, 2003: A technical guide to

MOM4, GFDL Ocean Group Tech. Rep. 5, NOAA/Geophysical Fluid Dynamics Laboratory, Princeton, NJ, 295 pp.

Griffies, S. M., et al., 2005: Formulation of an ocean model for global climate simulations. *Ocean Science*, **1**, 45–79.

Hall, A., 2004: The Role of Surface Albedo Feedback in Climate. *Journal of Climate*, **17**, 1550–1568.

Hansen, J., R. Ruedy, M. Sato, and K. Lo, 2010: Global surface temperature change. *Reviews of Geophysics*, **48**, RG4004.

Held, I. M. and B. J. Soden, 2006: Robust Responses of the Hydrological Cycle to Global Warming. *Journal of Climate*, **19**, 5686–5699.

Herweijer, C., R. Seager, M. Winton, and A. Clement, 2005: Why ocean heat transport warms the global mean climate. *Tellus*, **57A**, 662–675.

Holland, M. and C. Bitz, 2003: Polar amplification of climate change in coupled models. *Climate Dynamics*, **21**, 221–232.

Jourdain, N. C., B. Barnier, J. Molines, J. Chanut, N. Ferry, G. Garric, and L. Parent, 2010: Deep convection in the Labrador Sea, as captured by a global ocean reanalysis and regional downscaling, abstract OS54B-07 presented at Fall Meeting, AGU, San Francisco, Calif.

Knutti, R. and L. Tomassini, 2008: Constraints on the transient climate response from observed global temperature and ocean heat uptake. *Geophys. Res. Lett.*, **35**, L09 701.

Levermann, A., J. Mignot, S. Nawrath, and S. Rahmstorf, 2007: The role of Northern sea ice cover for the weakening of the thermohaline circulation under global warming. *Journal of Climate*, **20**, 4160–4171.

Lin, S. J., 2004: A "vertically Lagrangian" finite-volume dynamical core for global models. *Mon. Wea. Rev.*, **132**, 2293–2307.

Lu, J. and M. Cai, 2009: Seasonality of polar surface warming amplification in climate simulations. *Geophys. Res. Lett.*, **36**, L16 704.

Mahlstein, I. and R. Knutti, 2011: Ocean Heat Transport as a Cause for Model Uncertainty in Projected Arctic Warming. *Journal of Climate*, **24**, 1451–1460.

Manabe, S. and R. J. Stouffer, 1979: A CO_2-climate sensitivity study with a mathematical model of the global climate. *Nature*, **282 (5738)**, 491–493.

Manabe, S., R. J. Stouffer, M. J. Spelman, and K. Bryan, 1991: Transient Responses of a Coupled Ocean Atmosphere Model to Gradual Changes of Atmospheric CO_2. Part I. Annual Mean Response. *Journal of Climate*, **4 (8)**, 785–818.

Mayer, M. and L. Haimberger, 2011: Poleward atmospheric energy transports and their variability as evaluated from ECMWF reanalysis data. *Journal of Climate*.

Meehl, a. T. S., G.A., et al., 2007: Global climate projections. *In: Climate Change 2007: The Physical Science Basis. Contribution of Working Group I to the Fourth Assessment Report of the Intergovernmental Panel on Climate Change*, S. Solomon, D. Qin, M. Manning, Z. Chen, M. Marquis, K. Averyt, M. Tignor, and H. Miller, Eds., Cambridge University Press, Cambridge, United Kingdom and New York, NY, USA.

520 Meehl, G., G. Boer, C. Covey, M. Latif, and R. J. Stouffer, 2000: The Coupled Model
521 Intercomparison Project (CMIP). *Bulletin of the American Meteorological Society*, **81 (2)**,
522 313–318.

523 Peixoto, J. and A. Oort, (Eds.) , 1992: *Physics of Climate*. American Institute of Physics,
524 New York.

525 Raper, S. C., J. M. Gregory, and R. J. Stouffer, 2002: The role of climate sensitivity
526 and ocean heat uptake on AOGCM transient temperature response. *Journal of Climate*,
527 **15 (1)**, 124–130.

528 Screen, J. A. and I. Simmonds, 2010: The central role of diminishing sea ice in recent Arctic
529 temperature amplification. *Nature*, **464**, 1334–1337.

530 Stouffer, R. J., J. Russel, and M. J. Spelman, 2006a: Importance of oceanic heat uptake in
531 transient climate change. *Geophys. Res. Lett.*, **33**, L17 704.

532 Stouffer, R. J., et al., 2006b: GFDL's CM2 Global Coupled Climate Models. Part IV:
533 Idealized Climate Response. *Journal of Climate*, **19 (5)**, 723–740.

534 Stouffer, R. J., et al., 2006c: Investigating the Causes of the Response of the Thermohaline
535 Circulation to Past and Future Climate Changes. *Journal of Climate*, **19 (8)**, 1365–1387.

536 Trenberth, K. and D. C. Stepaniak, 2004: The flow of energy through the earth's climate
537 system. *Q. J. R. Meteorol. Soc.*, **130 (603)**, 2677–2701.

538 Trenberth, K. E. and J. M. Caron, 2001: Estimates of Meridional Atmosphere and Ocean
539 Heat Transports. *Journal of Climate*, **14 (16)**, 3433–3443.

Weaver, A. J., E. Michael, M. Kienast, and O. Saenko, 2007: Response of the Atlantic meridional overturning circulation to increasing atmospheric CO_2: Sensitivity to mean climate state. *Geophys. Res. Lett.*, **34**, L05 708.

Winton, M., 2006: Amplified Arctic climate change: What does surface albedo feedback have to do with it? *Geophys. Res. Lett.*, **33**, L03 701.

Winton, M., 2008: Sea ice - Albedo feedback and nonlinear Arctic climate change. *Arctic Sea Ice Decline*, American Geophysical Union, 111–131.

Winton, M., 2011: Do climate models underestimate the sensitivity of northern hemisphere sea ice cover? *Journal of Climate*, in press.

Winton, M., K. Takahashi, and I. Held, 2010: Importance of Ocean heat Uptake Efficacy to Transient Climate Change. *Journal of Climate*, 2333 – 2344.

Wittenberg, A. T., A. Rosati, N.-C. Lau, and J. J. Ploshay, 2006: GFDL's CM2 Global Coupled Climate Models. Part III: Tropical Pacific Climate and ENSO. *Journal of Climate*, **19 (5)**, 698–722.

Wood, R. A., A. B. Keen, J. F. B. Mitchell, and J. M. Gregory, 1999: Changing spatial structure of the thermohaline circulation in response to atmospheric CO_2 forcing in a climate model. *Nature*, **399**, 572–575.

Xie, P. and G. K. Vallis, 2011: The Passive and Active Nature of Ocean Heat Uptake in Idealized Climate Change Experiments. *Climate Dynamics*, in press.

559 Zelinka, M. D. and D. L. Hartmann, 2011: Climate Feedbacks and their Implications for
560 Poleward Energy Flux Changes. *Journal of Climate*.

List of Tables

1 Model components 30

2 Sensitivities of the models using one hundred year averaged differences of the 1% CO_2/yr forced and control run. As discussed in Section 2b one can multiply all entries by 1.4 to approximate the widely used transient response. Last row: AMOC is the total North Atlantic meridional volume transport at 40°N of the forced run initial state and → around the year 140 in Sverdrups, and the reduction in percentage. Single entries and abbreviations are defined and discussed in Section 3b. 31

3 Top of the atmosphere shortwave perturbation (TOA SW) over the 40–90°N region and perturbation differences split up into the surface albedo feedback (SAF) and non-SAF contributions, in W/m^2. Net TOA is positive downward and perturbation means the hundred year averaged difference of the 1% CO_2/yr forced and control run. 32

TABLE 1. Model components

	CM2.0	CM2.1	ESM2preG	ESM2G
atmosphere	AM2 B-grid	AM2.1 finite volume		
ocean	MOM4 different tunings		GOLD different tunings	
land	LM2		LM3 different tunings	
ice	different tunings — SIS — same tuning			

TABLE 2. Sensitivities of the models using one hundred year averaged differences of the 1% CO_2/yr forced and control run. As discussed in Section 2b one can multiply all entries by 1.4 to approximate the widely used transient response. Last row: AMOC is the total North Atlantic meridional volume transport at 40°N of the forced run initial state and → around the year 140 in Sverdrups, and the reduction in percentage. Single entries and abbreviations are defined and discussed in Section 3b.

	unit	CM2.0	CM2.1	ESM2preG	ESM2G
global/40N-90N ΔT_s	K	1.163/1.915	1.058/1.578	1.181/1.896	0.834/1.137
global OHU	W/m^2	0.756	0.816	0.86	0.821
global OHU efficiency	W/m^2K	0.650	0.771	0.728	0.984
40N-90N/90S-40N OHU efficiency	PW/K	0.051/0.269	0.127/0.276	0.120/0.259	0.213/0.296
NH ice reduction eff.	$10^{12}m^2/K$	-1.468	-1.342	-1.694	-0.851
initial → reduced AMOC	Sv/%	17 → 13/24	26 → 14/ 46	15 → 8/47	22 → 10/55

TABLE 3. Top of the atmosphere shortwave perturbation (TOA SW) over the 40–90°N region and perturbation differences split up into the surface albedo feedback (SAF) and non-SAF contributions, in W/m^2. Net TOA is positive downward and perturbation means the hundred year averaged difference of the 1% CO_2/yr forced and control run.

	net TOA SW	= surface + non-surface
ΔCM2.0 – ΔCM2.1 (Figure 7a)	0.15	= 0.38 – 0.23
ΔESM2preG – ΔESM2G (Figure 7b)	1.24	= 0.84 + 0.4

List of Figures

1 Processes associated with high latitude heat budget. 35

2 Upper panel: Mean fluxes of our four models in their control climate state. Lower panel: Mean flux perturbations for the same models (1% CO_2/yr forced minus control run) under 2.5 W/m^2 global CO_2 forcing. All fluxes are described in W/m^2 where the area is the Earth's surface between 40 and 90°N. The sum of the fluxes in the atmospheric and oceanic box are only close to zero since the mean of four models is shown. For each individual model they are balanced (not shown). Abbreviations are defined in Figure 1. 36

3 Time series of the simulated maximum North Atlantic meridional overturning circulation strength at 40°N of the 1% CO_2/yr forced run, in Sverdrups ($10^6 m^3 s^{-1}$), 5 year running mean, detailed description in Section 3. The time of CO_2 doubling and quadrupling is indicated in year 70 and 140, respectively. ESM2G (black), ESM2preG (red), CM2.1 (blue), CM2.0 (green). 37

4 Zonally integrated perturbation of oceanic northward heat transport in Petawatt. Perturbation means the difference between the hundred year averaged 1% CO_2/yr forced and control run. ESM2G (black), ESM2preG (red), CM2.1 (blue), CM2.0 (green). The vertical black line indicates the lower boundary used for the analysis of the high latitude heat budget. 38

5 North Atlantic close-up of the hundred year averaged wintertime (JFM) mixed layer depth in meters for the control climate (top four panels) and the perturbation, i.e., 1% CO_2/yr forced minus control run (lower four panels, different color coding) as a measure of convection. The Labrador Sea convection is only reduced in the models with substantial control climate Labrador Sea convection (right hand side). 39

6 Zonal mean atmosphere and ocean temperature perturbation, i.e., 1% CO_2/yr forced minus control run in Kelvin for CM2.0 (upper left), ESM2preG (lower left), CM2.1 (upper right) and ESM2G (lower right). The two models on the right hand side are the ones which have Labrador Sea convection. 40

7 Forcing of the difference in hundred year averaged northern high latitude temperature perturbation, i.e., 1% CO_2/yr forced minus control run. Upper panel ΔCM2.0 $-$ ΔCM2.1, lower panel ΔESM2preG $-$ ΔESM2G. Fluxes are described in W/m^2 where the area is the Earth's surface between 40 and 90°N. 41

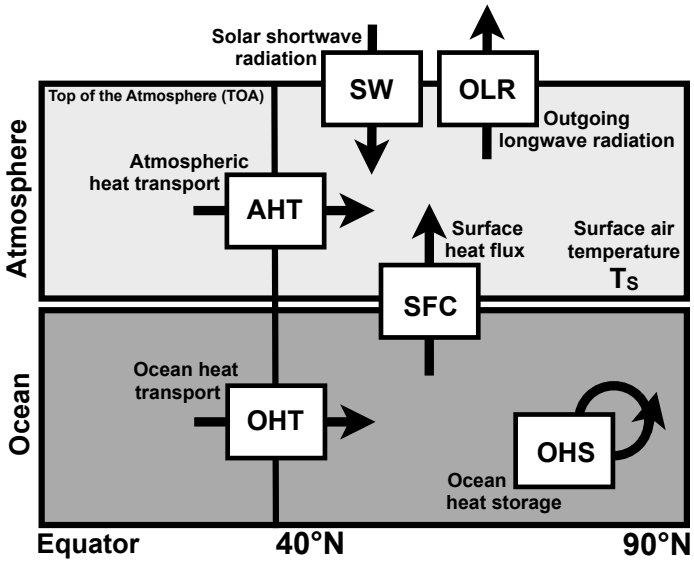

FIG. 1. Processes associated with high latitude heat budget.

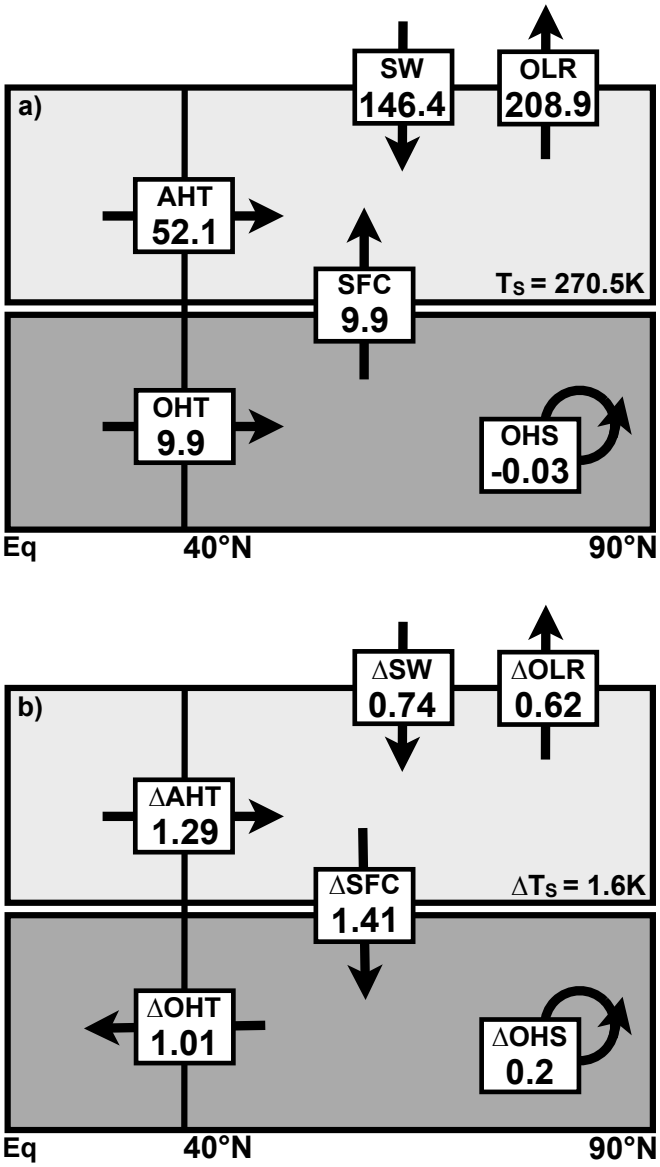

FIG. 2. Upper panel: Mean fluxes of our four models in their control climate state. Lower panel: Mean flux perturbations for the same models (1% CO_2/yr forced minus control run) under 2.5 W/m^2 global CO_2 forcing. All fluxes are described in W/m^2 where the area is the Earth's surface between 40 and 90°N. The sum of the fluxes in the atmospheric and oceanic box are only close to zero since the mean of four models is shown. For each individual model they are balanced (not shown). Abbreviations are defined in Figure 1.

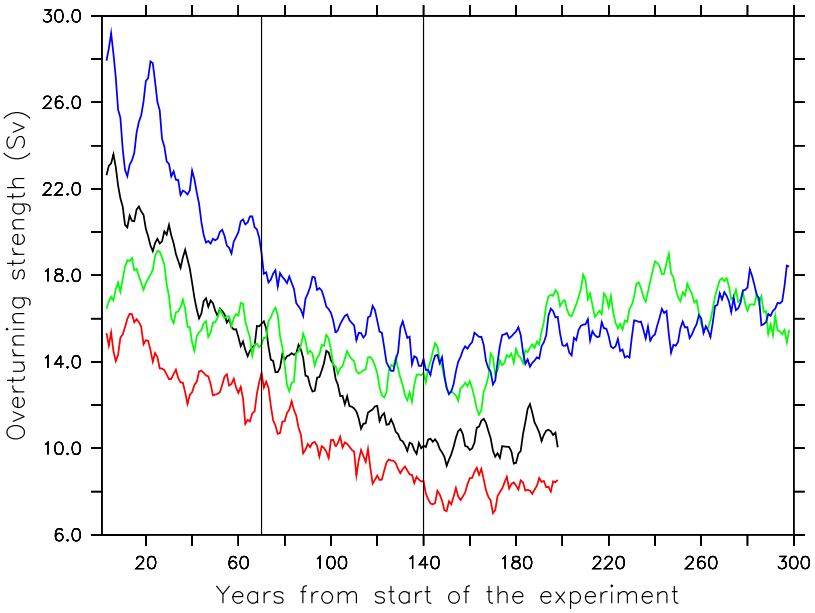

FIG. 3. Time series of the simulated maximum North Atlantic meridional overturning circulation strength at 40°N of the 1% CO_2/yr forced run, in Sverdrups ($10^6 m^3 s^{-1}$), 5 year running mean, detailed description in Section 3. The time of CO_2 doubling and quadrupling is indicated in year 70 and 140, respectively. ESM2G (black), ESM2preG (red), CM2.1 (blue), CM2.0 (green).

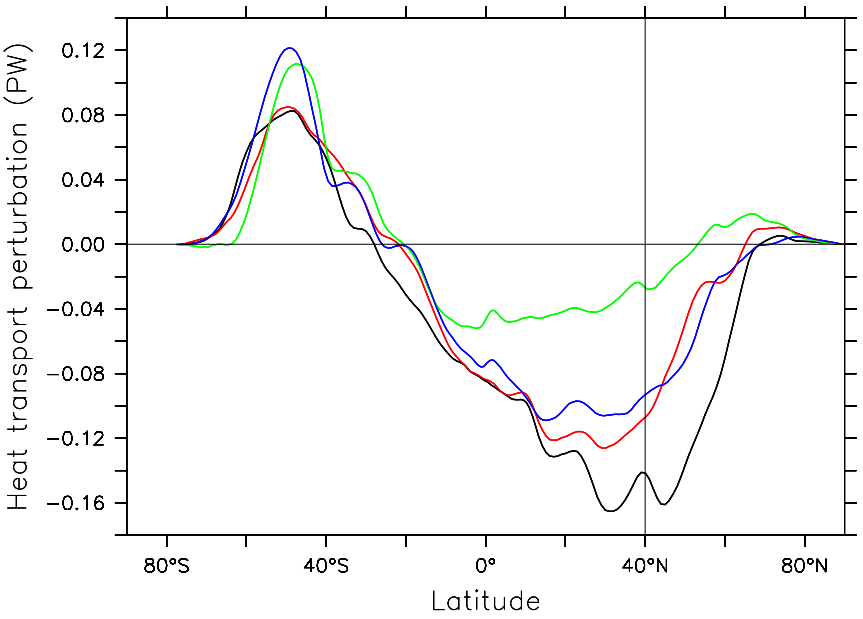

FIG. 4. Zonally integrated perturbation of oceanic northward heat transport in Petawatt. Perturbation means the difference between the hundred year averaged 1% CO_2/yr forced and control run. ESM2G (black), ESM2preG (red), CM2.1 (blue), CM2.0 (green). The vertical black line indicates the lower boundary used for the analysis of the high latitude heat budget.

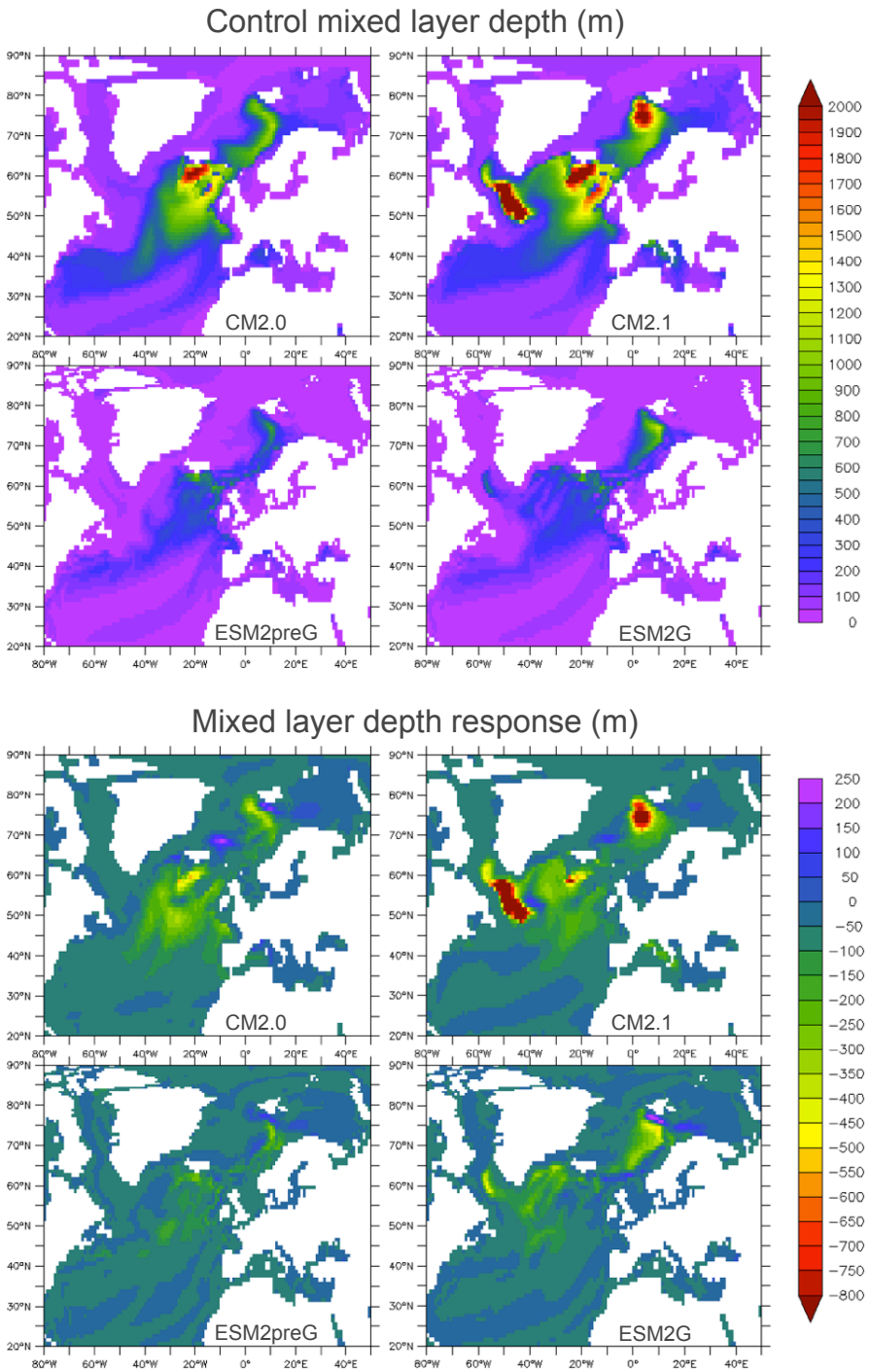

FIG. 5. North Atlantic close-up of the hundred year averaged wintertime (JFM) mixed layer depth in meters for the control climate (top four panels) and the perturbation, i.e., 1% CO_2/yr forced minus control run (lower four panels, different color coding) as a measure of convection. The Labrador Sea convection is only reduced in the models with substantial control climate Labrador Sea convection (right hand side).

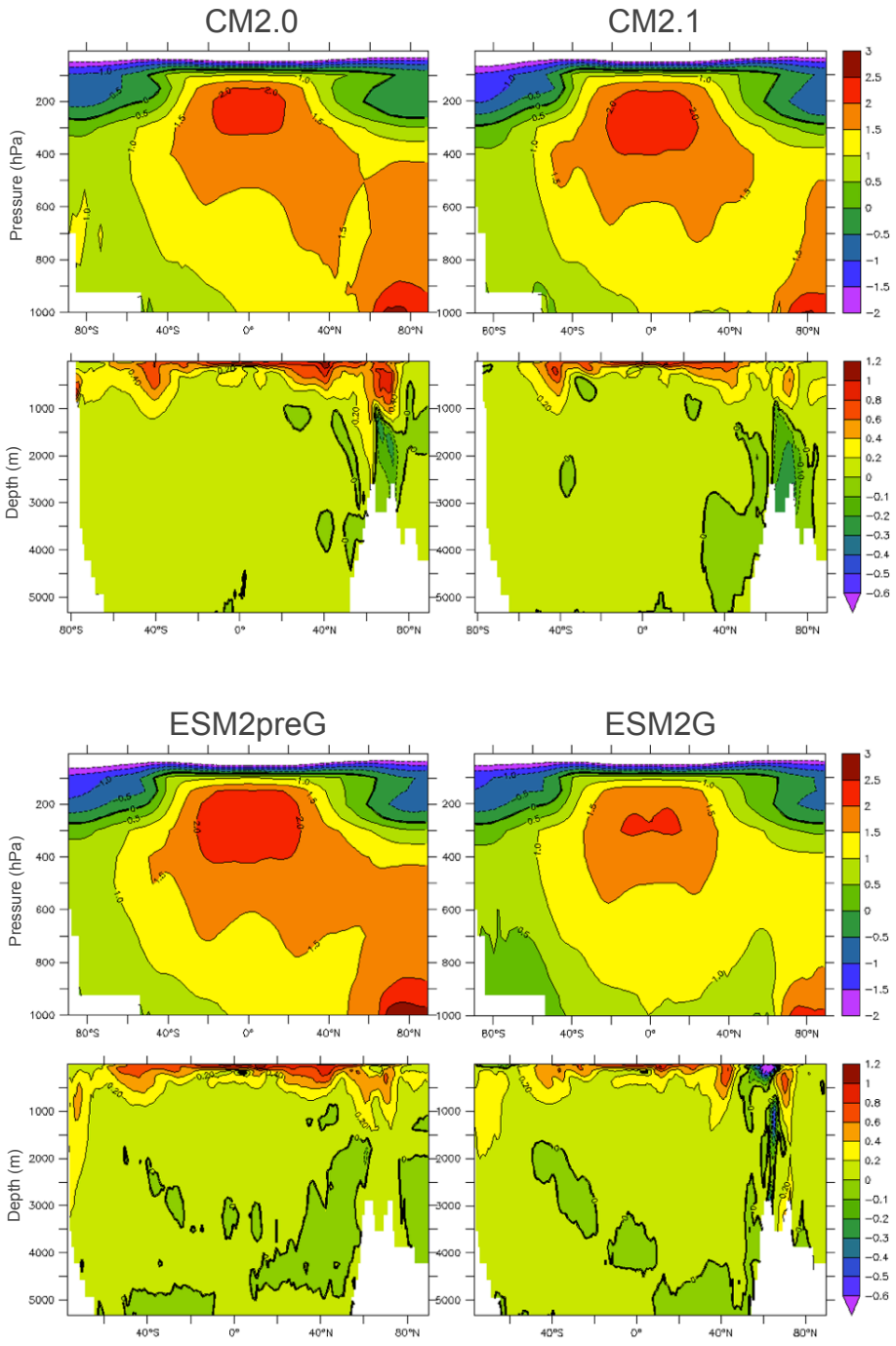

FIG. 6. Zonal mean atmosphere and ocean temperature perturbation, i.e., 1% CO_2/yr forced minus control run in Kelvin for CM2.0 (upper left), ESM2preG (lower left), CM2.1 (upper right) and ESM2G (lower right). The two models on the right hand side are the ones which have Labrador Sea convection.

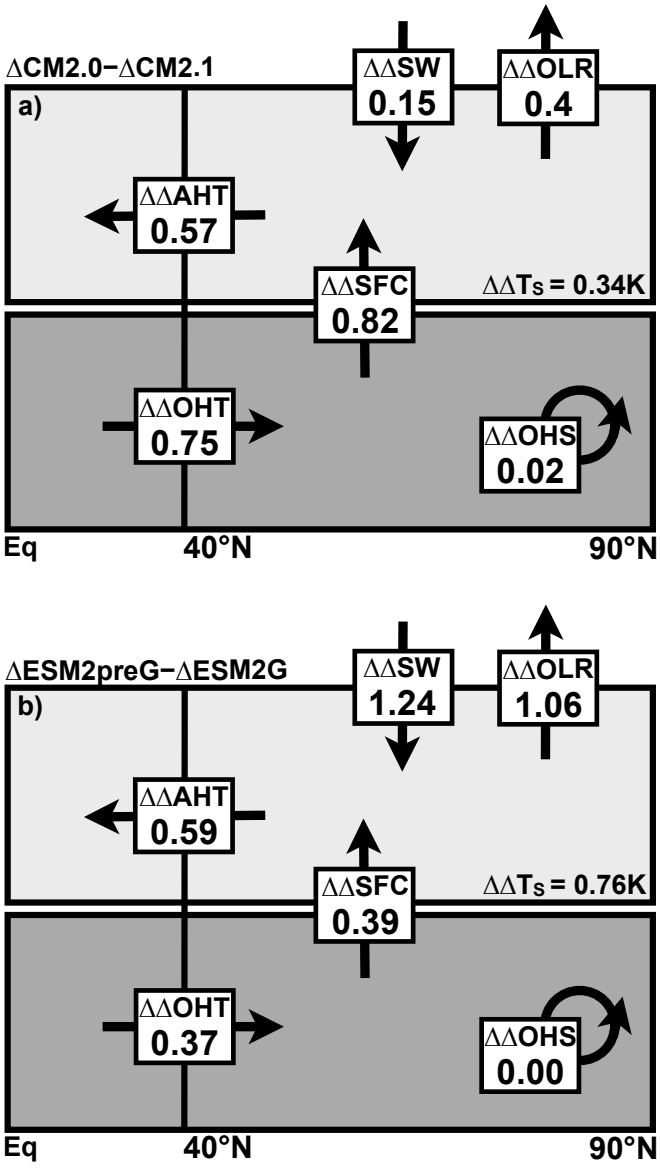

FIG. 7. Forcing of the difference in hundred year averaged northern high latitude temperature perturbation, i.e., 1% CO_2/yr forced minus control run. Upper panel ΔCM2.0 − ΔCM2.1, lower panel ΔESM2preG − ΔESM2G. Fluxes are described in W/m^2 where the area is the Earth's surface between 40 and 90°N.